

## Flux and spectral variation characteristics of 3C 454.3 at the GeV band

Hai-Ming Zhang<sup>1</sup>, Jin Zhang<sup>2</sup>, Rui-Jing Lu<sup>1</sup>, Ting-Feng Yi<sup>3</sup>, Xiao-Li Huang<sup>1</sup> and En-Wei Liang<sup>1</sup>

<sup>1</sup> Guangxi Key Laboratory for Relativistic Astrophysics, Department of Physics, Guangxi University, Nanning 530004, China

<sup>2</sup> Key Laboratory of Space Astronomy and Technology, National Astronomical Observatories, Chinese Academy of Sciences, Beijing 100101, China; [jinzhang@bao.ac.cn](mailto:jinzhang@bao.ac.cn)

<sup>3</sup> Department of Physics, Yunnan Normal University, Kunming 650500, China

Received 2017 December 3; accepted 2017 December 15

**Abstract** We analyze the long-term lightcurve of 3C 454.3 observed with *Fermi*/LAT and investigate its relation to flux in the radio, optical and X-ray bands. By fitting the 1-day binned GeV lightcurve with multiple Gaussian functions (MGF), we propose that the typical variability timescale in the GeV band is 1–10 d. The GeV flux variation is accompanied by the spectral variation characterized as flux-tracking, i.e., “harder when brighter.” The GeV flux is correlated with the optical and X-ray fluxes, and a weak correlation between  $\gamma$ -ray flux and radio flux is also observed. The  $\gamma$ -ray flux is not correlated with the optical linear polarization degree for the global lightcurves, but they show a correlation for the lightcurves before MJD 56000. The power density spectrum of the global lightcurve shows an obvious turnover at  $\sim 7.7$  d, which may indicate a typical variability timescale of 3C 454.3 in the  $\gamma$ -ray band. This is also consistent with the derived timescales by fitting the global lightcurve with MGF. The spectral evolution and an increase in the optical linear polarization degree along with the increase in  $\gamma$ -ray flux may indicate that the radiation particles are accelerated and the magnetic field is ordered by the shock processes during the outbursts. In addition, the nature of 3C 454.3 may be consistent with a self-organized criticality system, similar to Sagittarius A\*, and thus the outbursts could be from plasmoid ejections driven by magnetic reconnection. This may further support the idea that the jet radiation regions are magnetized.

**Key words:** gamma rays: galaxies — galaxies: jets — quasars: individual (3C 454.3)

### 1 INTRODUCTION

Variabilities in multi-wavelength with timescales from one year to several hours, or even as short as a few minutes in the GeV-TeV band in some extreme cases, are observed in blazars (e.g., Fossati et al. 2008; Abdo et al. 2010; Aleksić et al. 2011; Arlen et al. 2013; Liao et al. 2016; Hong et al. 2017). The physical origin of the variability is still debated. The variability may be related to activities of the central engine, e.g., a newly-emerging component (Arlen et al. 2013; Jorstad et al. 2013), or a change in the jet’s physical properties, e.g., variations of Lorentz factors and particle acceleration mechanisms (Villata et al. 2007; Raiteri et al. 2011; Nalewajko 2013;

Zhu et al. 2016), or the geometric mechanism, e.g., fractal helical structure jets (Larionov et al. 2010), or an emission blob smaller than the jet cross section, e.g., ‘jet-in-jet’ or spine-layer model (e.g., Ghisellini & Tavecchio 2008; Chen 2017). A quasi-periodic oscillation (QPO), such as the 12-year QPO in OJ 287, was proposed due to a binary system of supermassive black holes in the center (Sillanpaa et al. 1988, 1996; Lehto & Valtonen 1996).

The flux variation is always accompanied by spectral variation. This may shed light on the particle acceleration and properties of the radiation regions. The observed relations between spectral index and flux in blazars are diverse. Cui (2004) reported that the spectral evolution behaviors of Mrk 421 in the X-ray band are very com-

plex and different during different flares. An increase in the synchrotron peak flux along with the increase in its peak position is observed in Mrk 421 and the other four TeV BL Lacs (PKS 0548–322, 1H 1426+418, Mrk 501 and 1ES 1959+650, Massaro et al. 2008; Tramacere et al. 2009), and a similar feature has also been reported in multi-wavelength radiation mechanism research on blazars (Zhang et al. 2012, 2013). However, Nalewajko (2013) did not find a common feature of spectral variation in the GeV band in a sample of the 40 brightest  $\gamma$ -ray flares observed by *Fermi*/LAT.

3C 454.3 is one of the most active blazars in multi-wavelengths from radio to  $\gamma$ -ray bands (Ackermann et al. 2010; Jorstad et al. 2010, 2013; Raiteri et al. 2011; Wehrle et al. 2012; Britto et al. 2016). An extraordinary outburst at the  $\gamma$ -ray band in December 2009 was observed with *Fermi*/LAT, which made 3C 454.3 the brightest  $\gamma$ -ray source in the sky for over one week, and since then several brighter outbursts in the  $\gamma$ -ray band were detected by *Fermi*/LAT (Ackermann et al. 2010; Pacciani et al. 2014; Britto et al. 2016). By observing the parsec-scale jet in 3C 454.3 with the Very Long Baseline Array (VLBA) during its pronounced flaring in 2005–2008, Jorstad et al. (2010) suggested that a superluminal knot emerges from the core, which generated a series of optical and high-energy outbursts. A similar phenomenon was observed again in 3C 454.3 during its  $\gamma$ -ray outbursts in 2009 and 2010 (Jorstad et al. 2013). These factors may imply that the variability of 3C 454.3 is connected with its central engine activities.

In this paper, we present a comprehensive analysis of the GeV emission from 3C 454.3 with the *Fermi*/LAT observation data and investigate its relation to emission in X-ray, optical and radio bands. The reduction of the *Fermi*/LAT data is given in Section 2. Variability behaviors in the GeV band are described in Section 3. Using the well-sampled observation data of *Fermi*/LAT, we investigate the spectral evolution in the GeV band in Section 4. The cross-correlation analysis of variability among multiple wavelength lightcurves is presented in Section 5. A discussion and summary are reported in Section 6 and Section 7, respectively.

## 2 FERMILAT DATA REDUCTION

The data observed with *Fermi*/LAT (Pass 8 data) from 2008 August 6 (Modified Julian Day, MJD 54684) to 2016 February 16 (MJD 57434) for 3C 454.3 are used

in our analysis. The temporal coverage of the data is 7.5 yr. Our data analysis is performed with the standard analysis tool *gtlike/pyLikelihood*, which is part of the *Fermi* Science Tools software package<sup>1</sup> (ver. v10r0p5). The P8R2-SOURCE-V6 set of instrument response functions was used.

Photons with energies from 0.1 to 200 GeV are taken into account for our analysis. The significance of the  $\gamma$ -ray signal from the source is evaluated with the maximum-likelihood test statistic (TS), where the events with  $TS \geq 21$  are taken. They are selected from the region of interest with radius of  $10^\circ$ , centered at the position of 3C 454.3. The Galactic longitude and latitude are  $86.1^\circ$  and  $-38.2^\circ$ , respectively. The isotropic background, including the sum of residual instrumental background and extragalactic diffuse  $\gamma$ -ray background, is fitted with a model derived from the isotropic background at high Galactic latitude, i.e., “iso-P8R2-SOURCE-V6-v06.txt,” and the Galactic diffuse GeV emission is modeled with “gll-iem-v06.fits”<sup>2</sup>. In order to eliminate contamination from the  $\gamma$ -ray-bright Earth limb, the events with zenith angle larger than  $100^\circ$  are excluded.

A power-law spectral model is used to fit the observed spectrum in each time bin with an unbinned maximum likelihood method, i.e.,

$$\frac{dN}{dE} = \frac{N(\Gamma + 1)E^\Gamma}{E_{\max}^{\Gamma+1} - E_{\min}^{\Gamma+1}}, \quad (1)$$

where  $\Gamma$  is the photon spectral index for events in the energy band between  $E_{\min}$  (0.1 GeV) and  $E_{\max}$  (200 GeV).

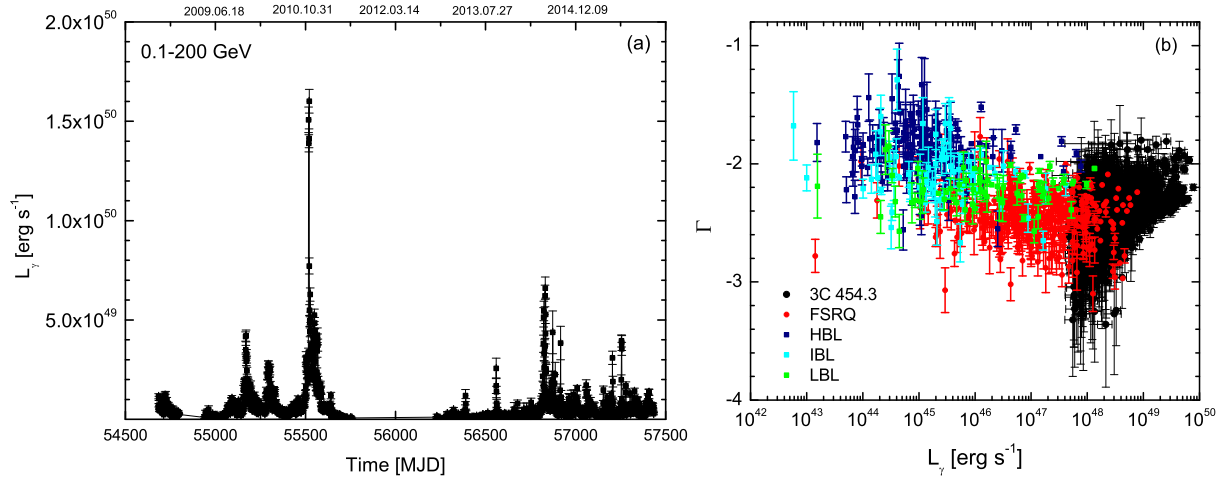
## 3 VARIABILITY IN THE GEV BAND

Figure 1(a) shows the derived LAT lightcurve of 3C 454.3 in a time bin of 1 d. Note that no observational data with  $TS \geq 21$  are available in the time intervals from MJD 54797 to MJD 54939 and from MJD 55758 to MJD 56228. One can observe that 3C 454.3 experienced several violent outbursts in the  $\gamma$ -ray band during the past  $\sim 8$  yr. An extremely bright flare is observed with the highest luminosity of  $1.60 \pm 0.06 \times 10^{50} \text{ erg s}^{-1}$  on 2010 November 20 (MJD 55520), which erupts at  $\sim$  MJD 55478 and returns to the quiet state at  $\sim$  MJD 55594, lasting more than three months with three other obvious flare peaks.

<sup>1</sup> <https://fermi.gsfc.nasa.gov/ssc/data/analysis/software/>

<sup>2</sup> Taken from

<http://fermi.gsfc.nasa.gov/ssc/data/access/lat/BackgroundModels.html>



**Fig. 1** Panel (a): Global lightcurve of 3C 454.3 in the GeV band, where the observed luminosity ( $L_\gamma$ ) is the integral luminosity of the *Fermi*/LAT energy band (from 100 MeV to 200 GeV). Panel (b):  $\Gamma$  as a function of  $L_\gamma$  for 3C 454.3. The data on blazars are taken from Ackermann et al. (2015), where HBL, IBL and LBL indicate high-frequency-peaked BL Lac, intermediate-frequency peaked BL Lac and low-frequency-peaked BL Lac, respectively.

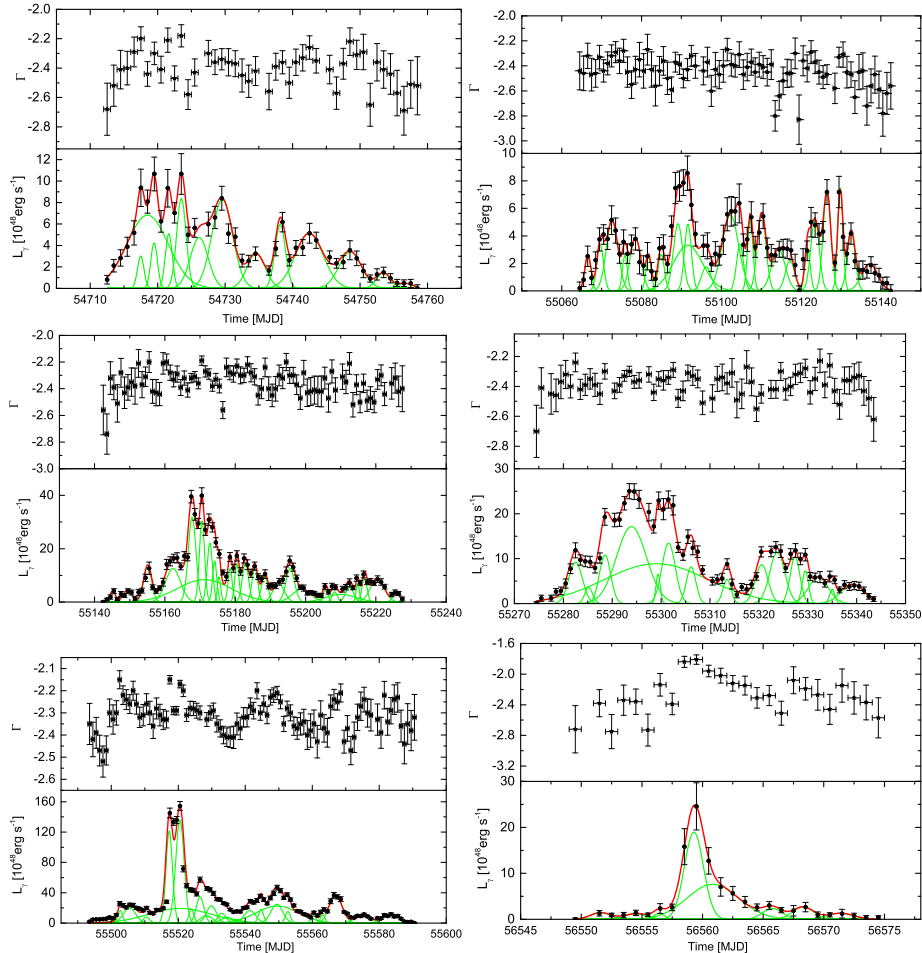


**Fig. 2** The daily lightcurves of luminosity and photon spectral index for 3C 454.3. The scattered points are observation data of *Fermi*/LAT. The thin green lines are derived by multiple Gaussian functions, and the thick red lines are the sum of all the Gaussian components. The values of FWHM,  $L_{\text{peak}}$  and  $E_\gamma$  for each Gaussian component are listed in Table 1.

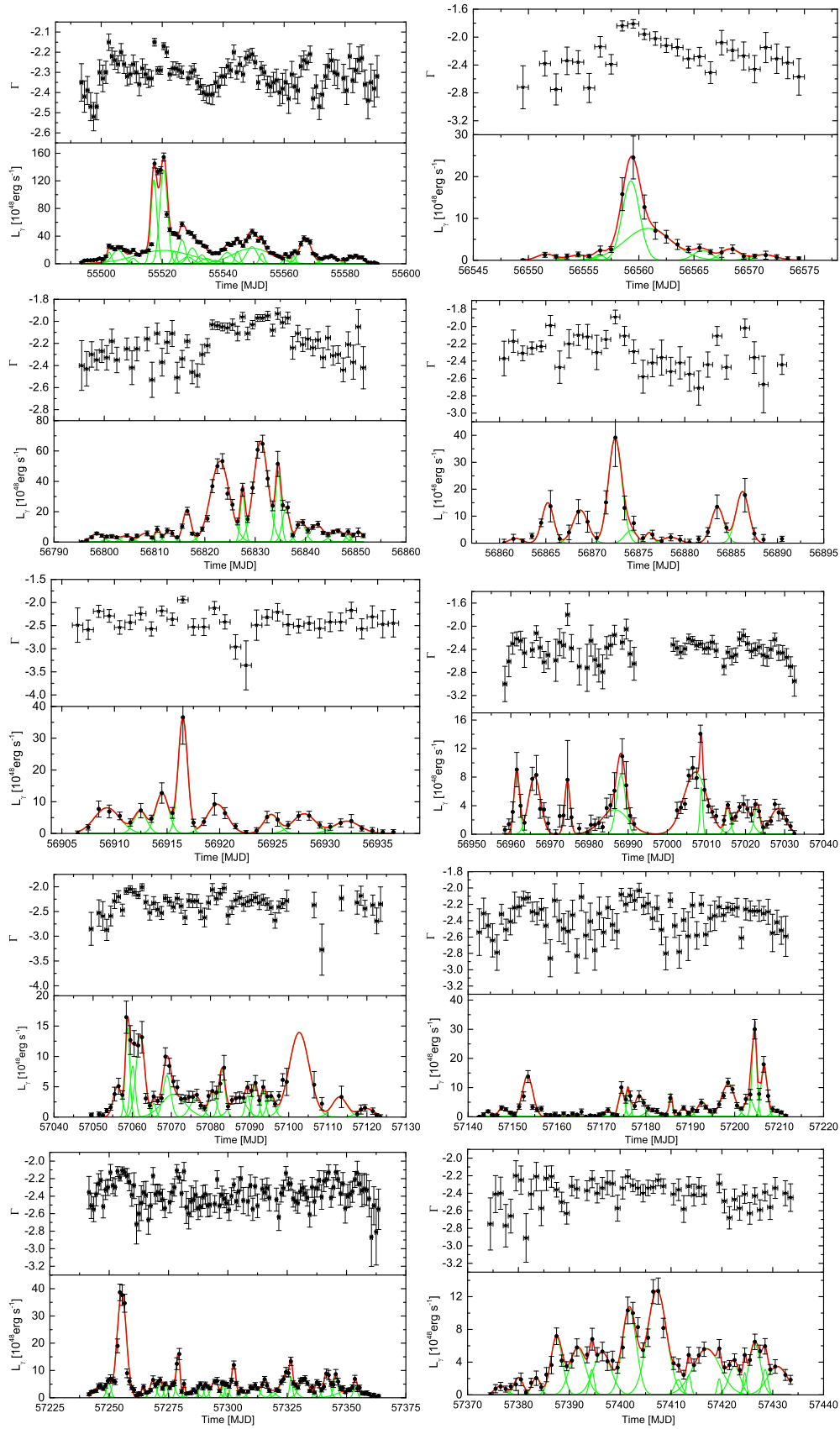
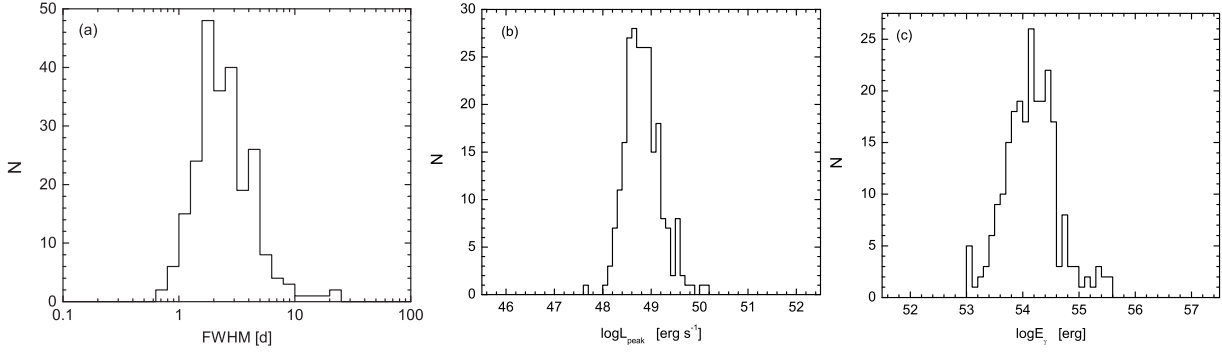
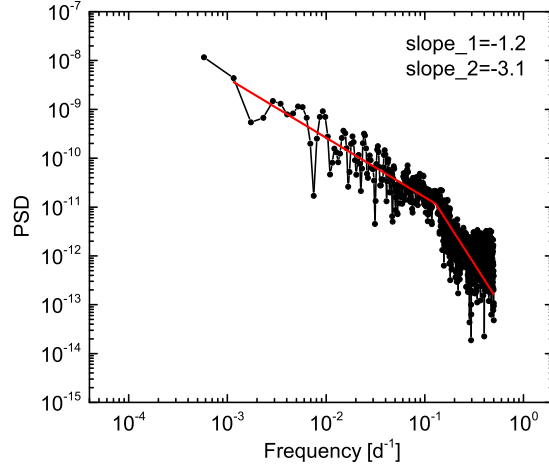


Fig. 2 — Continued.



**Fig. 3** Distributions of FWHM,  $L_{\text{peak}}$  and  $E_{\gamma}$  for these Gaussian components in Fig. 2.



**Fig. 4** PDS of the global lightcurve in the  $\gamma$ -ray band. The red line shows the fitting result with the broken power-law function.

Giant outbursts are composed of many flares. We divide the global GeV lightcurve into 14 outburst episodes in order to demonstrate these flares. We do not adopt a rigid criterion to select each episode. It usually starts at a time when the flux goes up from a baseline and ends at a time when the flux goes down to the baseline. Each episode is composed of several pulses. We fit the lightcurve of each episode with multiple Gaussian functions. Our results are shown in Figure 2. The global lightcurve during the 7.5 yr in the  $\gamma$ -ray band is fitted with 236 Gaussian components, corresponding to 236 flares. We calculate the full width at half maximum (FWHM), peak luminosity ( $L_{\text{peak}}$ ) and total radiation energy ( $E_{\gamma}$ ) of each flare, where  $E_{\gamma}$  is derived by the integrated emission in the duration of each Gaussian component in the 0.1–200 GeV energy band. The results are listed in Table 1.

Based on identifying flares with the Gaussian-fitting method, we also find that the GeV lightcurves in some

episodes are composed of two components, spiked flares with short-timescale and broad flares with long-timescale, as displayed in Figure 2. Most flares are spike flares. The FWHM values of the broad components usually span tens of days and they are dimmer than the spiked flares. It is possible that the two components are from different radiation regions.

The distributions of FWHM,  $L_{\text{peak}}$  and  $E_{\gamma}$  are exhibited in Figure 3. It is found that the FWHM values range from  $\sim 1$  d to  $\sim 25$  d, clustered at 2–5 d. Although the time-bin selection effect (1-day in this analysis) may lead a bias on the intrinsic FWHM distribution, it still indicates that the timescales of the GeV flares should be several days. The  $L_{\text{peak}}$  values of these flares range from  $10^{47.6} \text{ erg s}^{-1}$  to  $10^{50.2} \text{ erg s}^{-1}$  and narrowly cluster within  $10^{48.3} \text{--} 10^{49.2} \text{ erg s}^{-1}$ .  $E_{\gamma}$  ranges from  $10^{53.0}$  to  $10^{55.6} \text{ erg}$ , clustering at  $10^{53.6}$  to  $10^{54.6} \text{ erg}$ .

To further investigate the variability properties of 3C 454.3 in the GeV band, we calculate the power

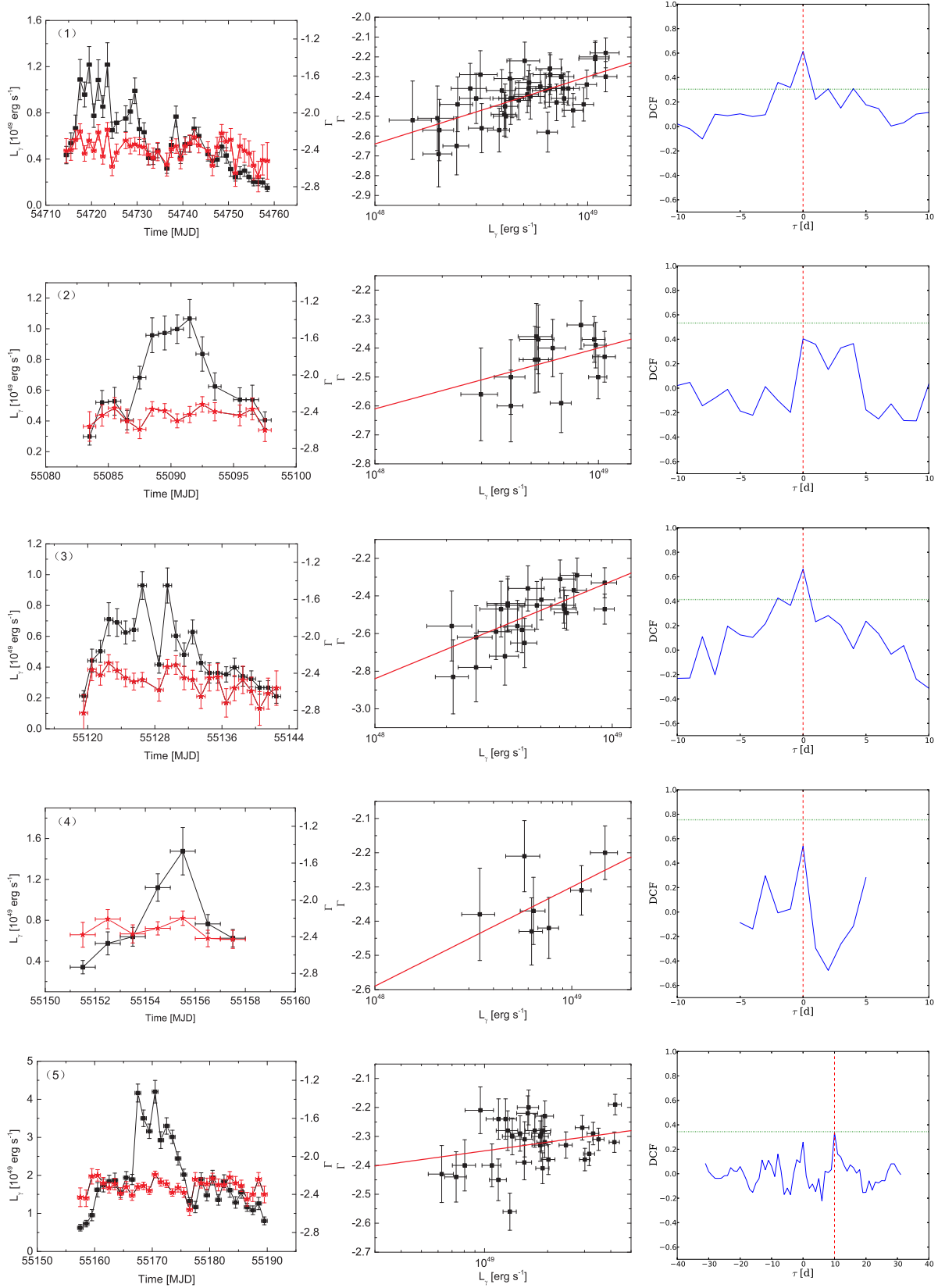


**Fig. 5** *Left Panels:* The temporal evolution of luminosity ( $L_\gamma$ , *black squares*) and photon spectral index ( $\Gamma$ , *red stars*) observed by *Fermi*/LAT for 3C 454.3. *Middle Panels:*  $\Gamma$  vs.  $L_\gamma$  for each outburst episode in the left panels. The *red lines* are the linear fitting lines by considering the errors of both  $\Gamma$  and  $L_\gamma$ , for which the slopes are listed in Table 2. *Right Panels:* The DCF results between  $\Gamma$  and  $L_\gamma$ , where  $\Gamma$  and  $L_\gamma$  have been normalized with the Min-Max Normalization method before the DCF analysis. The *green horizontal lines* represent the 95% confidence level.

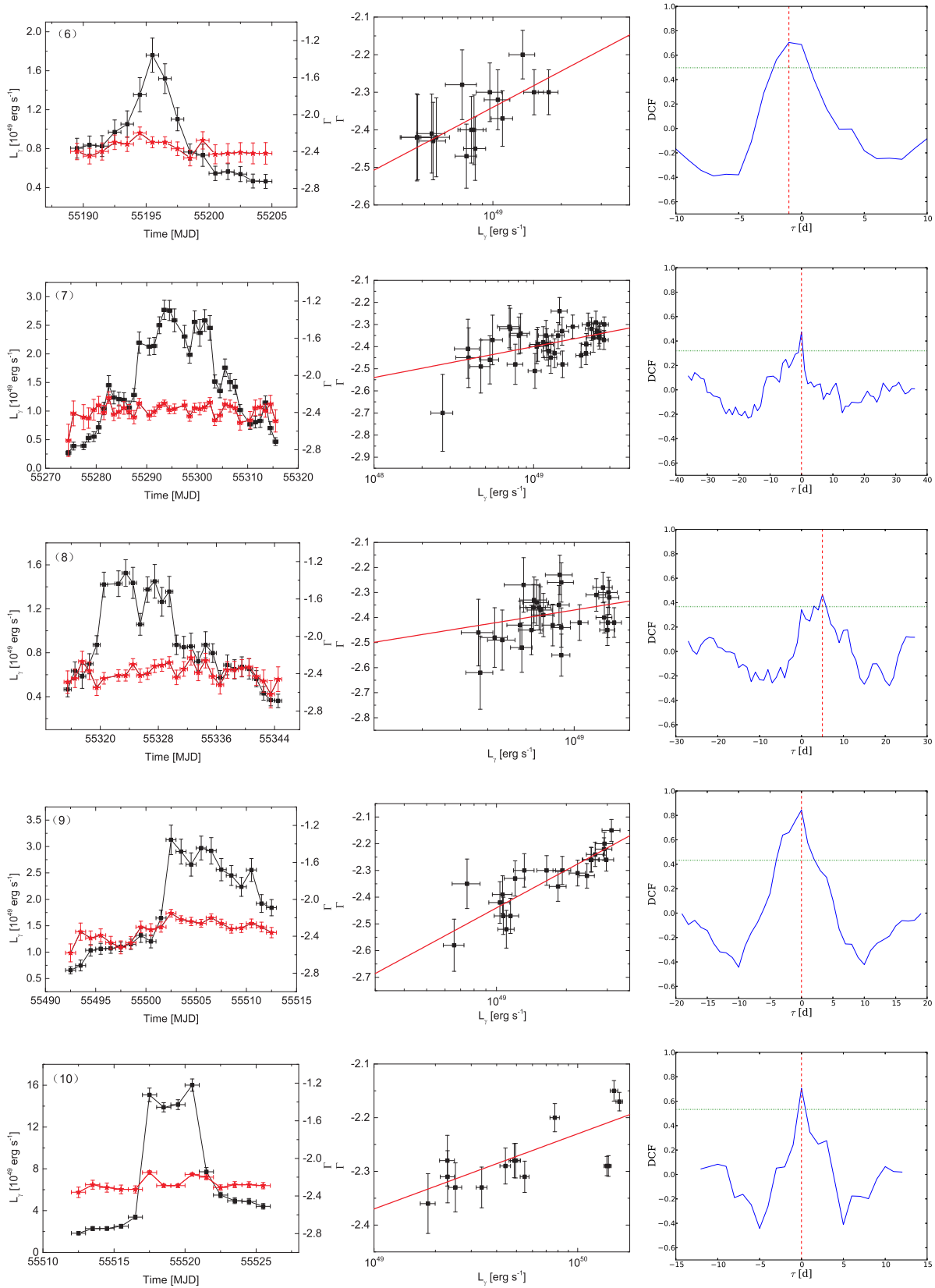


Fig. 5 — Continued.

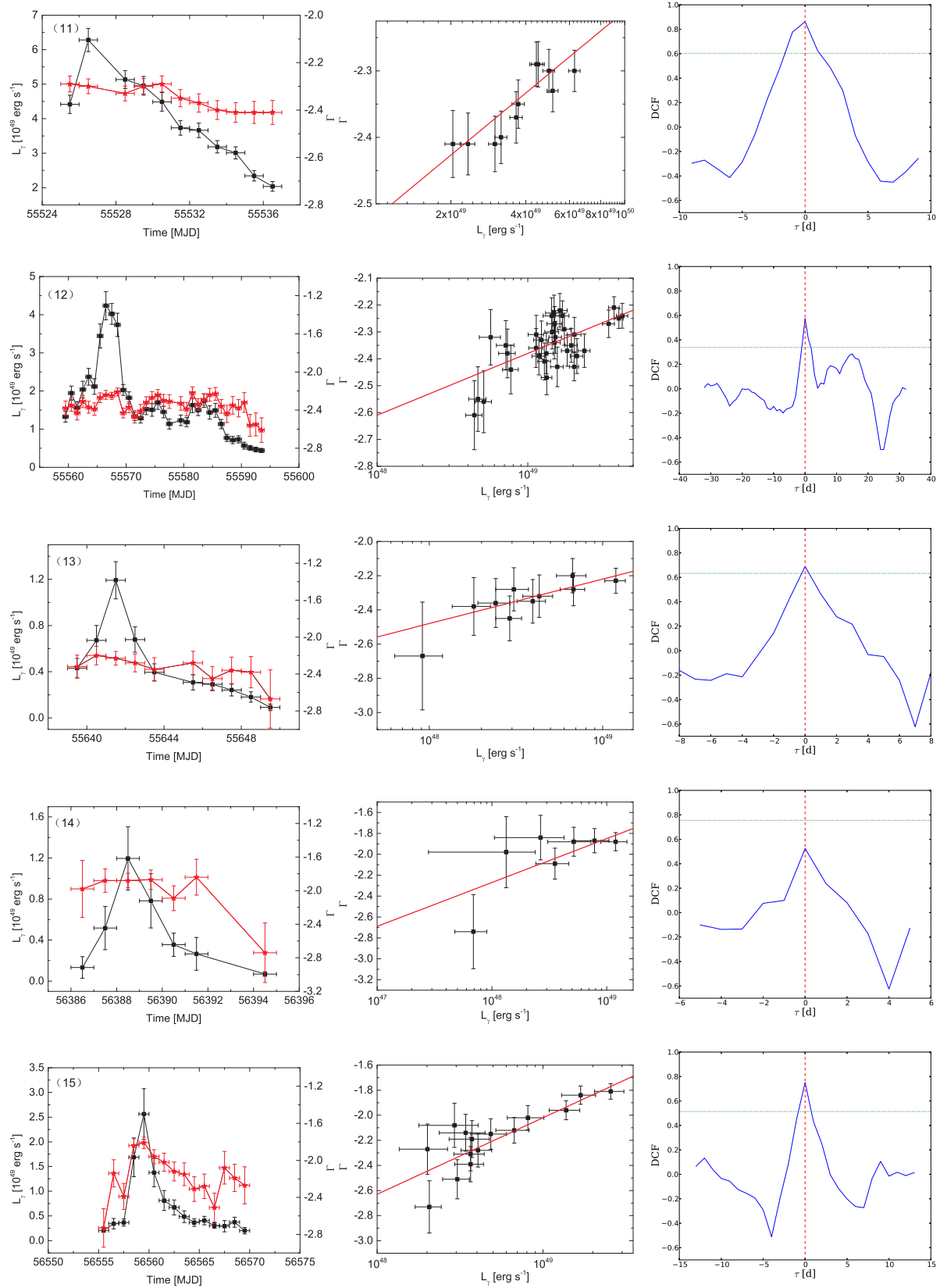


Fig. 5 — Continued.

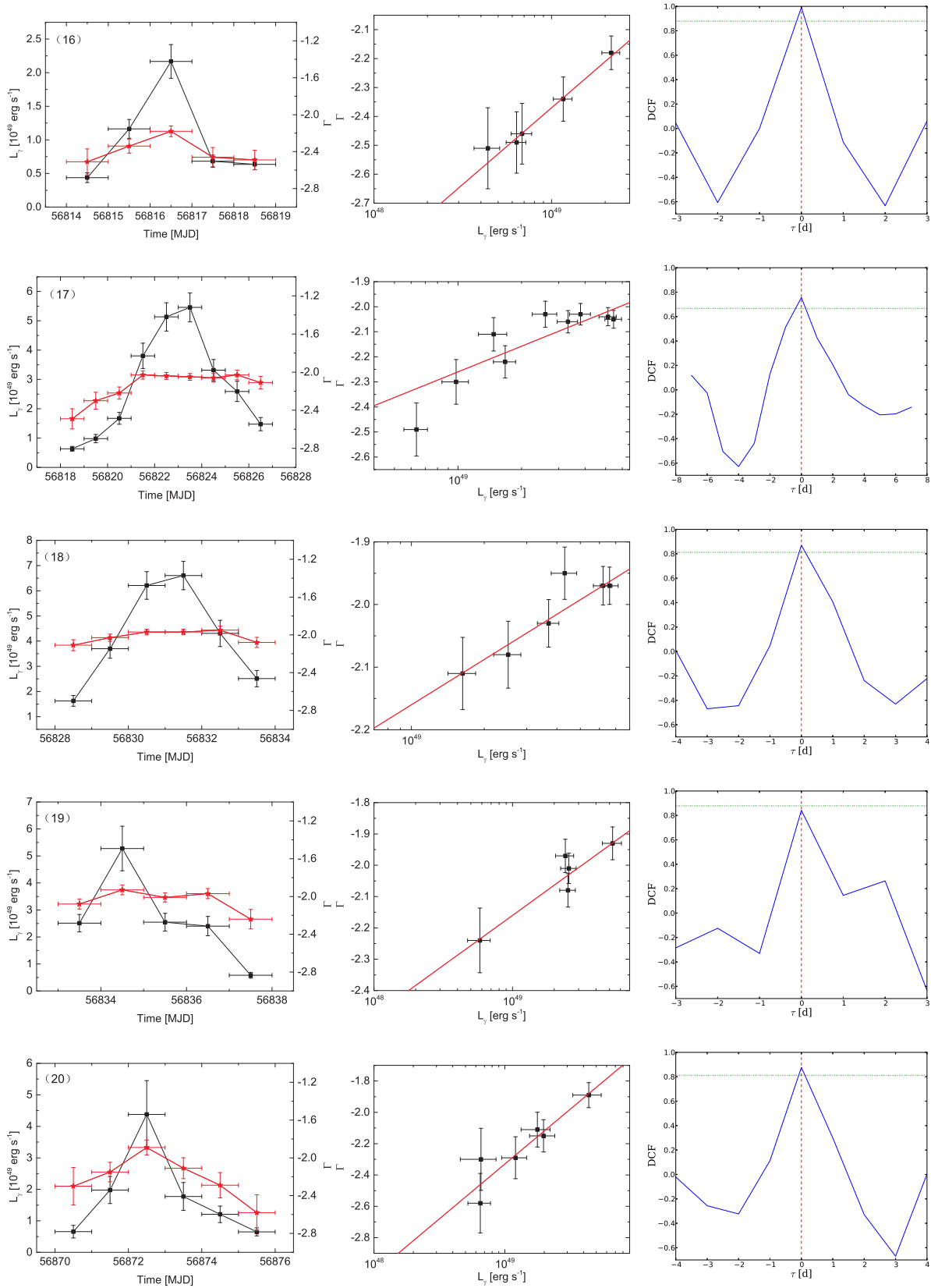


Fig. 5 — Continued.

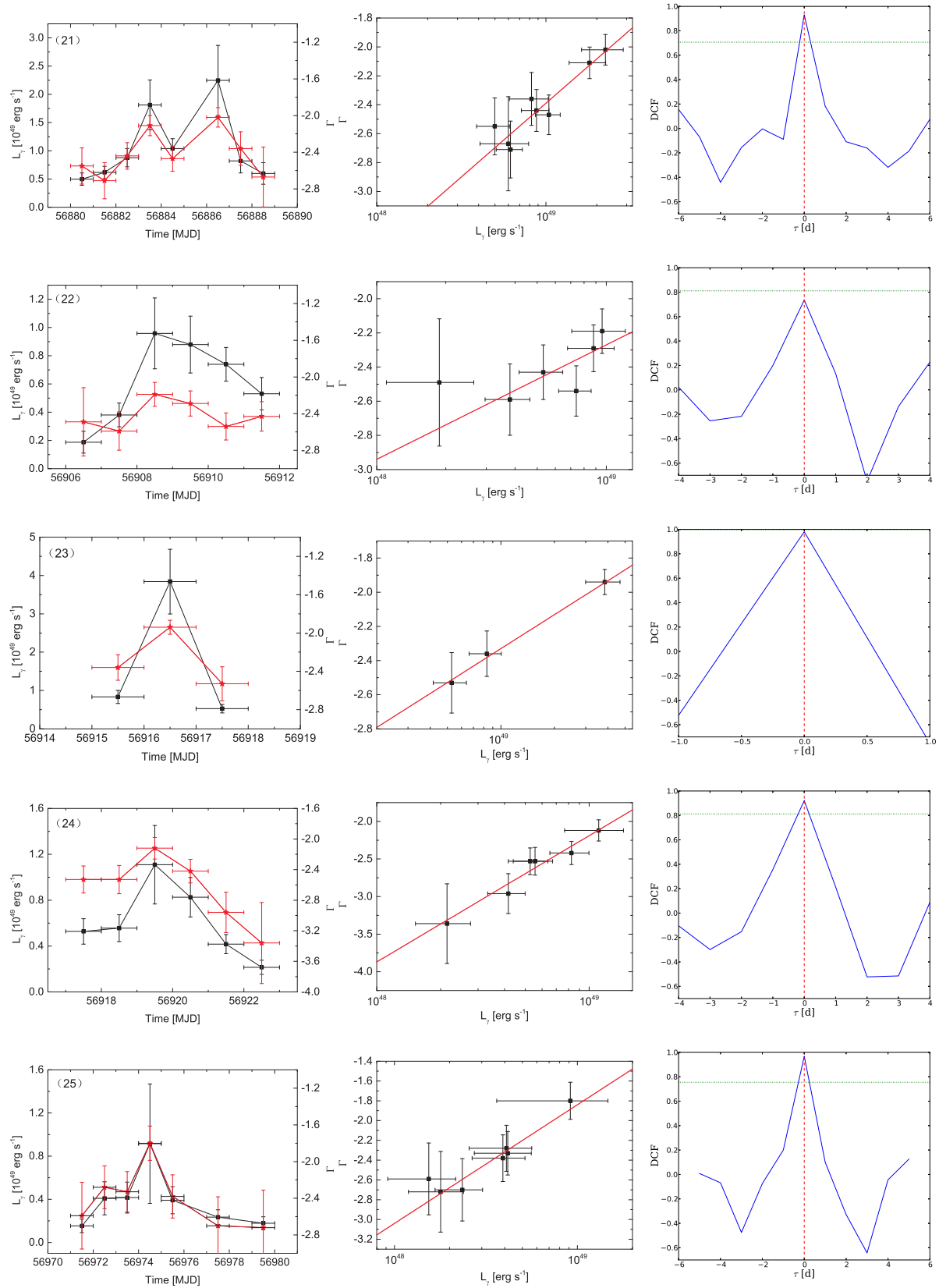


Fig. 5 — Continued.

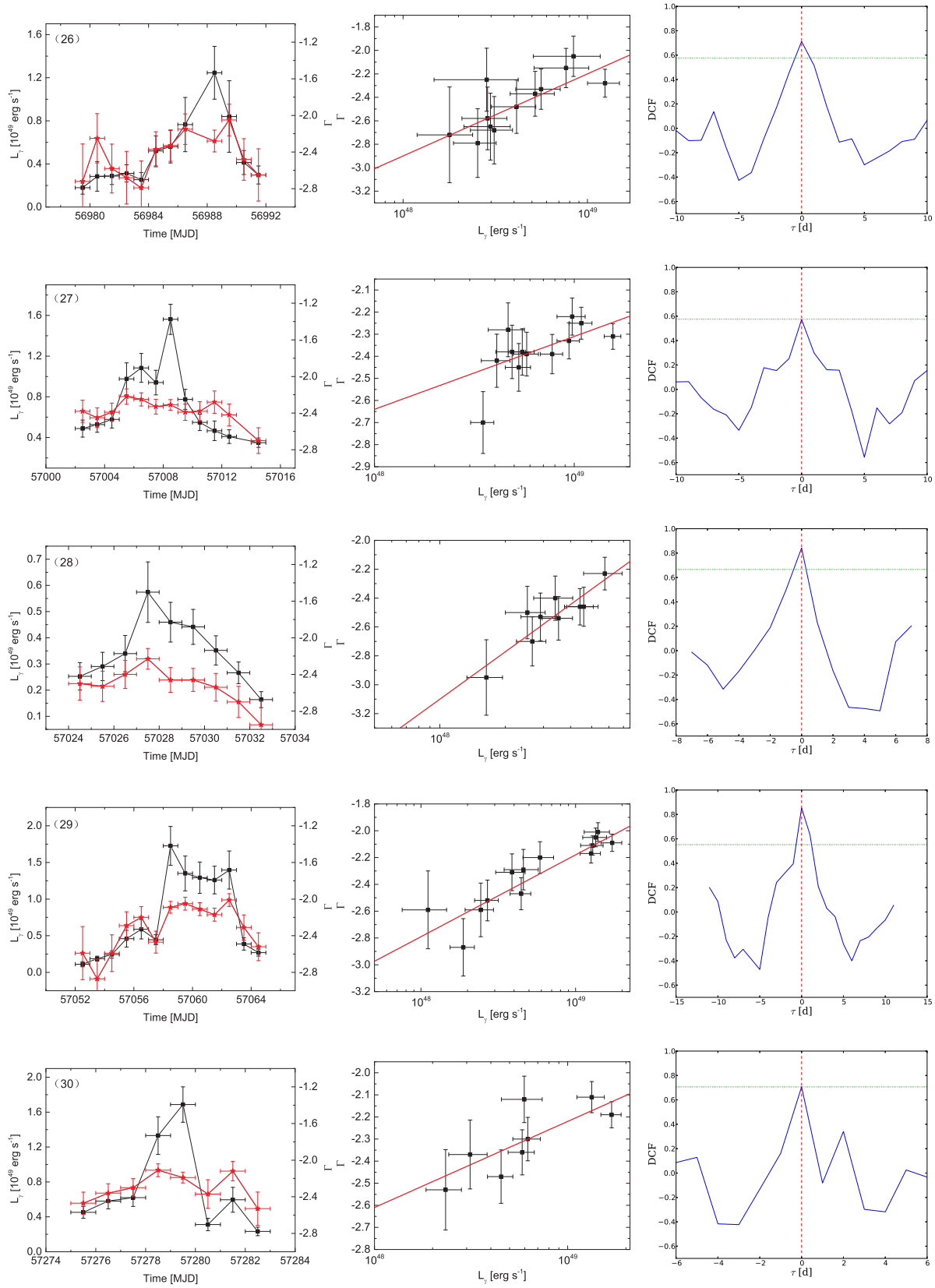


Fig. 5 — Continued.

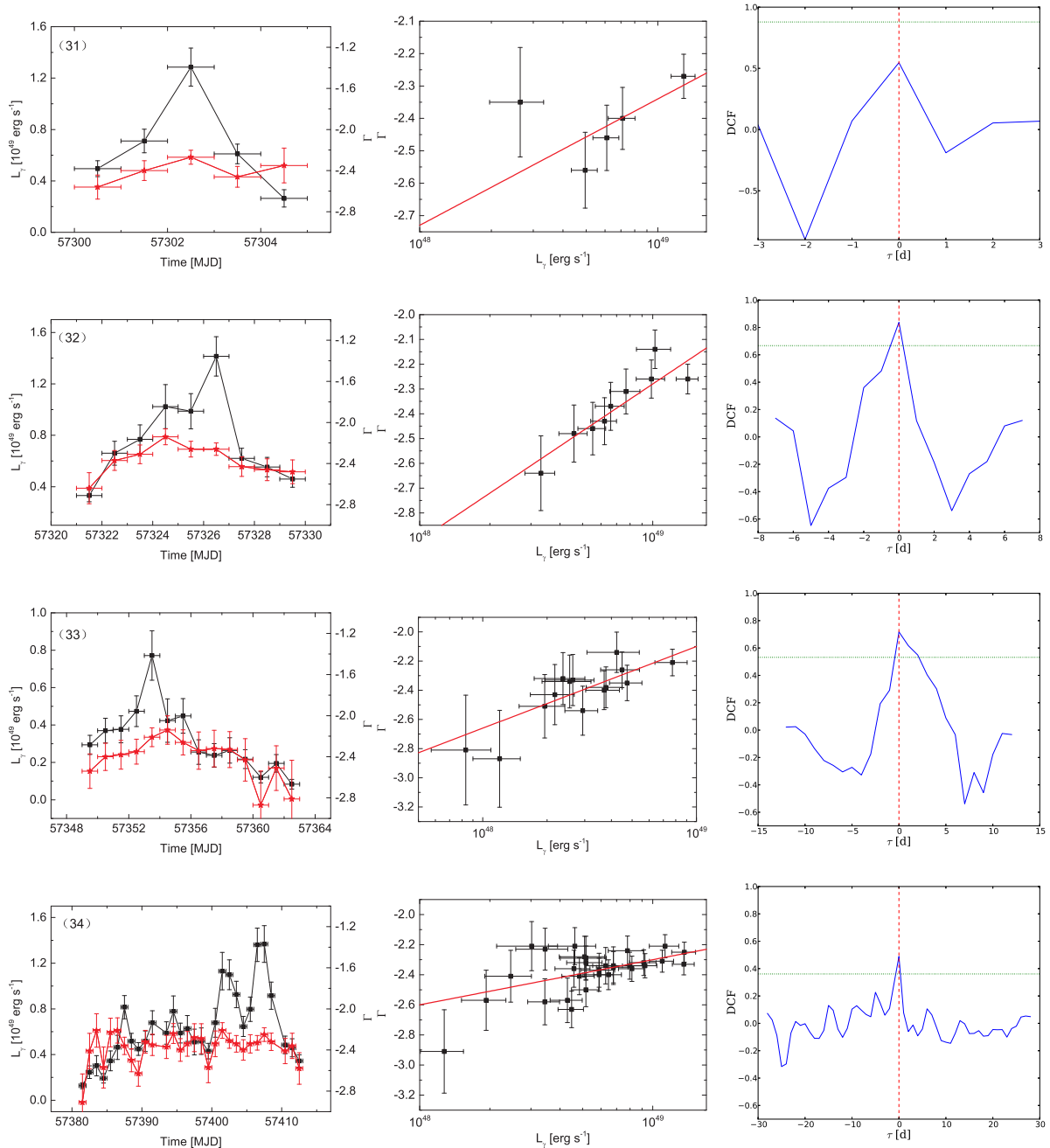


Fig. 5 — Continued.

density spectrum (PDS) of the global lightcurve in the GeV band with the Lomb-Scargle Periodogram algorithm (Lomb 1976; Scargle 1982). The PDS curve is shown in Figure 4. We use a broken power-law function to fit the PDS curve of 3C 454.3, and the posterior probability density of parameters in the model is derived by a Bayesian Markov chain Monte Carlo technique (Vaughan 2010). The derived turnover is at  $\sim 7.7$  d, which may correspond to a typical variability timescale

of 3C 454.3 in the GeV band. This is roughly consistent with the FWHM distribution.

#### 4 CORRELATIONS BETWEEN SPECTRAL INDEX AND FLUX VARIATIONS

Spectral index and flux variation may shed light on the particle acceleration and radiation physics.

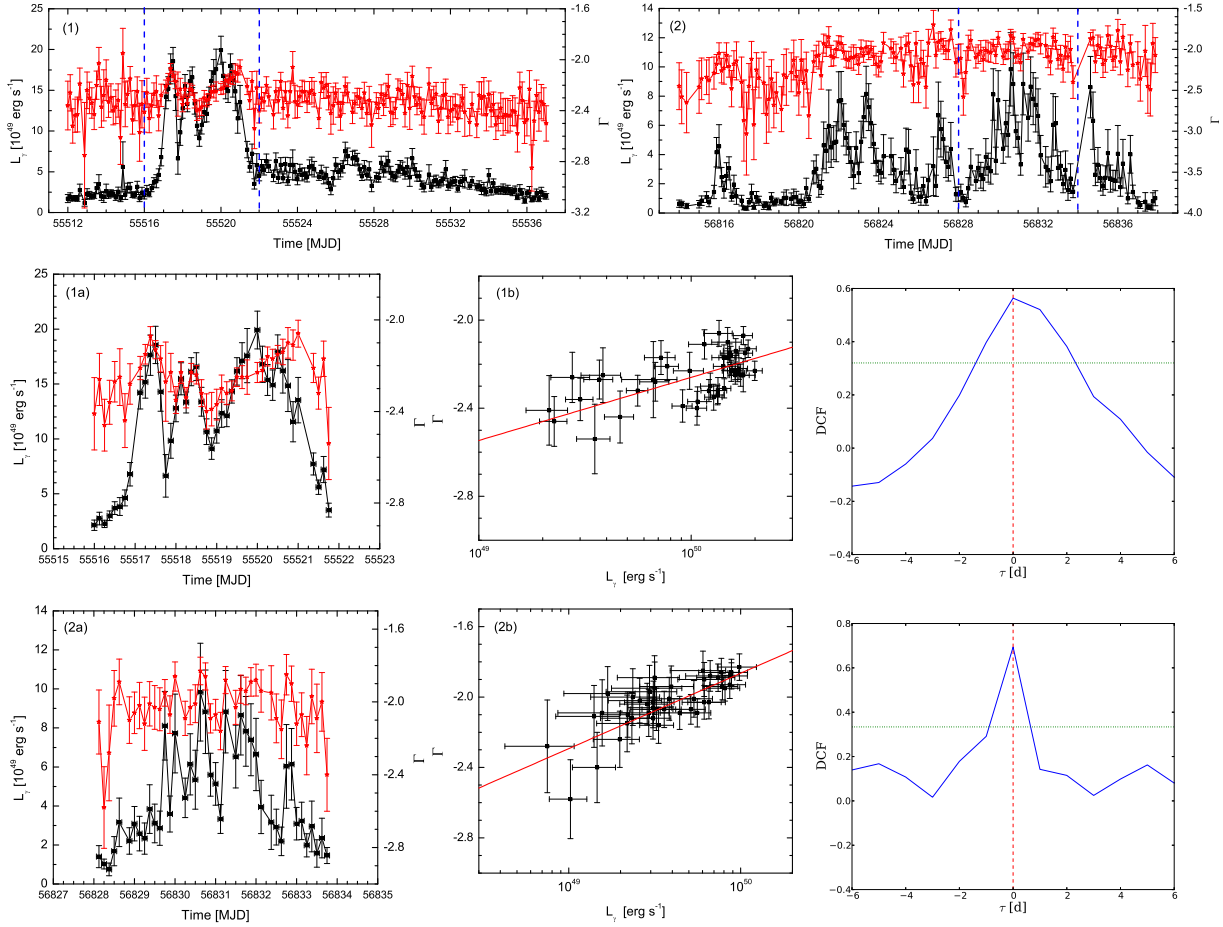


**Fig. 6** Top Panels: Temporal evolution of luminosity ( $L_\gamma$ , black squares) and photon spectral index ( $\Gamma$ , red stars) with 3-hour binning. Further analysis of the data between blue vertical dashed lines is presented in the lower panels; left panels: temporal evolution of  $L_\gamma$  (black squares) and  $\Gamma$  (red stars) with 3-hour binning. Middle panels:  $\Gamma$  vs.  $L_\gamma$  for two flares in the left panels. The red lines are the linear fitting lines by considering the errors of both  $\Gamma$  and  $L_\gamma$ . Right panels: DCF results between  $\Gamma$  and  $L_\gamma$ , where  $\Gamma$  and  $L_\gamma$  have been normalized with the Min-Max Normalization method before the DCF analysis. The green horizontal lines are the 95% confidence level lines.

Figure 2 also shows the temporal evolution of photon spectral index ( $\Gamma$ ) in the  $\gamma$ -ray band for each episode. One can find that the flux variation is accompanied by  $\Gamma$  variation.

Figure 1(b) illustrates the variation of 3C 454.3 in the  $L_\gamma$ - $\Gamma$  plane, where the *Fermi* blazars taken from Ackermann et al. (2015) (see also their fig. 14) are also presented in order to make a comparison. The data on 3C 454.3 are distributed in the high luminosity end in the  $L_\gamma$ - $\Gamma$  plane. Its  $\Gamma$  values range from  $-1.80 \pm 0.19$  (in MJD [56974, 56975]) to  $-3.36 \pm 0.53$  (in MJD [56922, 56923]), and are larger than  $-2$  in some bright flares, such as that observed in the episodes of MJD [56545, 56575], MJD [56790, 56852], MJD [56860, 56890] and MJD [56960, 57040].

Using the Pearson correlation analysis method, we analyze the correlation between  $L_\gamma$  and  $\Gamma$  for 3C 454.3 in different flux stages. A tentative correlation with a correlation coefficient of  $r = 0.46$  and a chance probability of  $p \sim 0$  is found. To further study this issue, we investigate the  $\Gamma - L_\gamma$  correlation in 34 bright outbursts, among them 6 outbursts have  $L_{\max}/L_{\min} \geq 10$ , 13 outbursts have  $5 \leq L_{\max}/L_{\min} < 10$  and 15 outbursts have  $3 \leq L_{\max}/L_{\min} < 5$ , where  $L_{\max}$  and  $L_{\min}$  are the maximum and minimum luminosities in the selected outbursts respectively. Note that we do not have a critical criterion to separate these outbursts. We only artificially select the time intervals that have bright flares. The maximum and minimum durations among the 34 outbursts are 45 d and 3 d, respectively. The values of  $L_{\max}$ ,  $L_{\min}$ ,

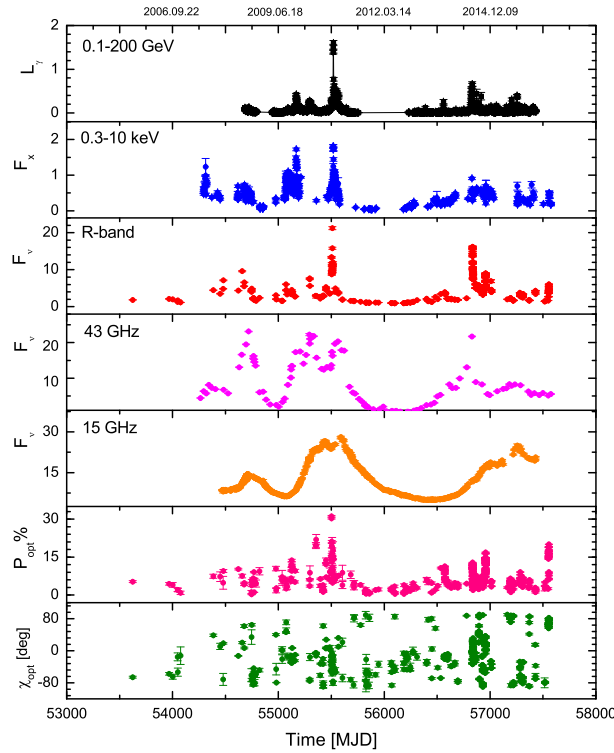


**Fig. 7** Lightcurves of 3C 454.3 in multi-wavelength. The LAT lightcurve is the same as in Fig. 1, in units of  $10^{50}$  erg  $s^{-1}$ . The X-ray data are obtained with observations of the *Swift* satellite (in units of  $10^{-10}$  erg  $cm^{-2}$   $s^{-1}$ ). The optical polarization and *R*-band data are taken from the 1.83 m Perkins Telescope at Lowell Observatory. The 43 GHz data are from the VLBA observation. The 15 GHz data are from the OVRO 40 m radio telescope.

$L_{\max}/L_{\min}$  as well as the duration of each outburst are reported in Table 2.

Figure 5 shows the temporal variations of  $L_{\gamma}$  and  $\Gamma$  as well as  $\Gamma$  as a function of  $L_{\gamma}$  for the 34 selected outbursts. Most outburst episodes exhibit a strong correlation between  $\Gamma$  and  $L_{\gamma}$ . The correlation coefficient and chance probability of the Pearson correlation analysis with slope of linear fits for each outburst episode are reported in Table 2, where the errors of both  $\Gamma$  and  $L_{\gamma}$  are considered during the linear fitting. These results indicate that the variations of luminosity are accompanied by spectral evolution in most of the outburst cases for 3C 454.3, showing the behavior of flux tracking as “harder when brighter.”

We also study the correlation and possible lag behavior between  $L_{\gamma}$  and  $\Gamma$  in each outburst episode using the discrete cross-correlation function (DCF, Edelson & Krolik 1988). The results of the DCF analysis are presented in the right panels of Figure 5. The correlation between  $L_{\gamma}$  and  $\Gamma$  for 28 outbursts is significant at over the 95% confidence level, and except for outburst episodes 5 (10 d), 6 (−1 d) and 8 (5 d), no lag behavior is found in other outburst episodes.

Note that the above analysis is based on the one-day binning of lightcurves. Fast variabilities on timescale of hours (or even shorter) have been reported for 3C 454.3 (Abdo et al. 2011; Britto et al. 2016). Therefore, we also re-analyze the two outbursts that have a peak luminosity  $L_{\gamma} > 5 \times 10^{49}$  erg  $s^{-1}$  in Figure 1(a) by using a time-bin of 3-hours. As illustrated in Figure 6, the statistical correlations between  $L_{\gamma}$  and  $\Gamma$  are still presented during the fast flares (see also Abdo et al. 2011; Britto et al. 2016). The Pearson correlation analysis yields  $r = 0.59$  with a chance probability of  $p = 3.1 \times 10^{-5}$  and  $r = 0.76$  with  $p = 6.0 \times 10^{-9}$  for the two flares, respectively. No lag behavior is found in the DCF analysis. These facts may imply that the behavior of “harder when brighter” is an intrinsic property of this source, which is independent of the size of the time-bin in the analysis.

## 5 CORRELATIONS OF EMISSION BETWEEN $\gamma$ -RAY AND OTHER ENERGY BANDS

The long-term simultaneously observed lightcurves of 3C 454.3 in X-ray, optical and radio at 43 GHz, as well as the polarization data are shown in Figure 7, which are

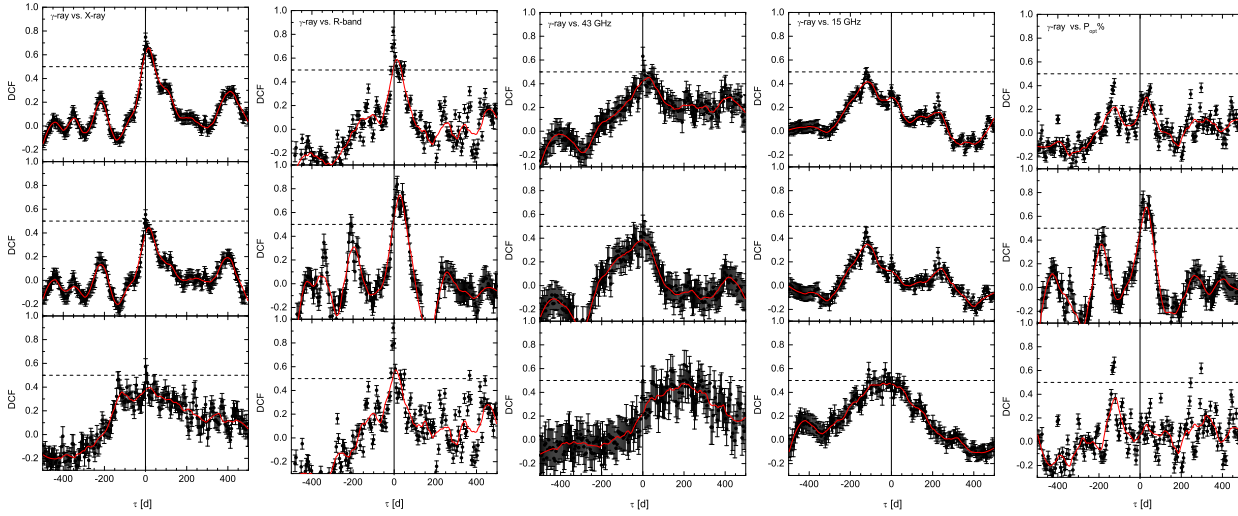


**Fig. 8** The DCF results of variability between  $\gamma$ -ray and other bands. The global lightcurves are divided into two segments at MJD 56000. The DCF results of variability are shown, for which the global lightcurves are given in top panels, the first segment lightcurves are given in middle panels, and the second segment lightcurves are given in bottom panels. The *vertical solid lines* and *horizontal dashed lines* indicate the lag of zero and the correlation coefficient of 0.5. The *red lines* are *smoothed lines* for the DCF curves.

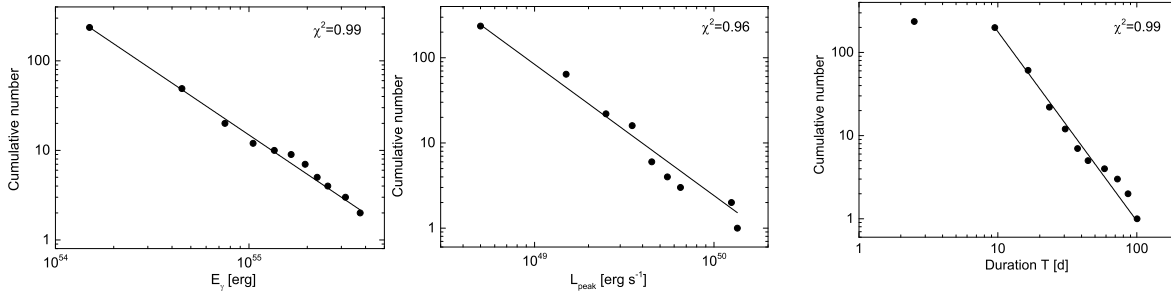


**Fig. 9** Cumulative distributions of energy ( $E_\gamma$ ), peak luminosity ( $L_{\text{peak}}$ ) and duration time ( $T$ ) for the  $\gamma$ -ray flares. They are fitted with a power-law function, and the derived slopes are  $\alpha_E = 1.46 \pm 0.02$ ,  $\alpha_L = 1.54 \pm 0.08$  and  $\alpha_T = 2.28 \pm 0.05$ , respectively.

taken from the website [http://www.bu.edu/blazars/VLBA project.html](http://www.bu.edu/blazars/VLBA_project.html); the X-ray data were collected from the *Swift* satellite. The optical photometric and polarization data are obtained with the 1.8 m Perkins Telescope at Lowell Observatory, and are not corrected for Galactic extinction. The 43 GHz data are compiled from VLBA observations. The radio data at 15 GHz that were obtained by the Owens Valley Radio Observatory (OVRO, <http://www.astro.caltech.edu/ovroblazars/>) 40 m radio telescope (Richards et al. 2011) are also displayed in Figure 7. The OVRO supports an ongoing blazar monitoring program in cooperation with the *Fermi* satellite program.

As illustrated in Figure 7, 3C 454.3 shows significant flux variation in multiple wavelengths. It was reported that its gamma-ray outbursts are usually accompanied by

flux variations in low-energy bands (e.g., Jorstad et al. 2013; Wehrle et al. 2012). In addition, its flux variation in the gamma-ray band is also observed to be correlated with variation of the optical polarization (Jorstad et al. 2010, 2013). We make the DCF analysis of variability between  $\gamma$ -ray and other energy bands using the long-term lightcurves in multiple wavelengths, as shown in Figure 8. The DCF results are calculated using the logarithm of the flux, which is less dominated by high flux values (see also Ackermann et al. 2010). Note that no observational data are available from MJD 55758 to MJD 56228 at the gamma-ray band and there is a very large outburst at  $\sim$  MJD 55520, hence we divide the global lightcurves into two segments with MJD 56000, and then we also calculate the DCF results for the two segments among multi-wavelength, respectively. The results are

**Table 1** Fitting Results of the Global Lightcurve with Multiple Gaussian Functions

Center (MJD)	FWHM (d)	$L_{\text{peak}}$ ( $10^{48} \text{ erg s}^{-1}$ )	$E_{\gamma}$ ( $10^{54} \text{ erg}$ )
54717.49	1.13	3.00	0.31
54718.50	7.23	6.83	4.43
54719.47	1.16	4.19	0.45
54721.65	1.20	5.09	0.56
54723.51	1.64	8.36	1.26
54726.16	3.11	4.74	1.36
54729.58	3.63	8.28	2.76
54734.59	3.18	3.24	0.95
54738.17	1.81	5.94	0.99
54742.46	4.86	5.14	2.3
54748.54	3.92	3.41	1.23
54753.46	2.42	1.43	0.32
54756.68	2.67	0.47	0.11
55066.56	1.79	2.64	0.43
55069.64	1.97	3.33	0.60
55072.63	3.42	5.17	1.62
55075.83	1.45	2.57	0.34
55078.47	3.20	3.88	1.14
55081.79	1.58	2.46	0.35
55084.92	1.86	2.66	0.46
55089.15	2.76	4.88	1.24
55091.63	8.63	3.33	2.64
55091.64	2.04	4.84	0.91
55096.24	2.87	1.75	0.46
55102.26	4.88	5.52	2.48
55104.70	2.07	3.38	0.64
55107.26	1.58	5.13	0.74
55110.10	2.52	5.64	1.31
55114.32	3.96	3.03	1.10
55117.21	2.77	2.20	0.56
55121.61	1.57	3.09	0.45
55123.47	2.48	5.21	1.19
55126.50	2.26	7.30	1.52
55129.83	1.52	7.48	1.05
55132.55	2.31	4.34	0.92
55137.20	4.68	1.97	0.85
55145.16	1.86	4.10	0.70
55149.31	2.84	4.41	1.15
55155.09	2.67	12.96	3.18
55162.30	5.01	12.56	5.79
55167.75	2.60	31.80	7.59
55170.55	1.76	30.28	4.90
55171.18	17.89	8.40	13.83
55172.78	1.79	21.99	3.62
55174.17	1.42	15.30	2.00
55175.41	1.12	9.34	0.96
55178.55	1.42	12.48	1.63
55180.48	1.42	14.43	1.89
55182.90	2.13	14.27	2.80
55185.59	1.89	12.87	2.24
55188.39	2.13	9.84	1.93
55192.34	3.78	6.89	2.40
55195.64	2.90	12.52	3.34
55198.84	6.13	4.78	2.69
55205.67	1.64	4.60	0.69
55208.28	1.77	3.80	0.62
55210.07	9.99	2.88	2.65
55212.51	2.67	5.55	1.37
55214.84	1.06	6.99	0.68
55216.77	1.71	9.04	1.43

**Table 1** — *Continued.*

Center (MJD)	FWHM (d)	$L_{\text{peak}}$ ( $10^{48} \text{ erg s}^{-1}$ )	$E_{\gamma}$ ( $10^{54} \text{ erg}$ )
55220.42	4.58	8.89	3.74
55225.84	2.18	3.66	0.71
55282.52	3.27	9.21	2.77
55285.19	1.88	3.58	0.62
55288.53	2.72	10.81	2.7
55293.94	7.24	17.12	11.41
55298.99	24.84	8.87	20.07
55299.39	1.04	6.5	0.62
55301.55	3.21	13.47	3.98
55306.15	2.29	8.15	1.72
55313.48	1.95	5.38	0.96
55320.58	3.11	8.66	2.48
55323.77	3.66	11.43	3.85
55327.4	2.35	10.44	2.26
55329.51	1.55	7.28	1.03
55332.17	4.78	5.85	2.57
55335.01	1.31	3.09	0.37
55339.24	5.66	4.29	2.15
55502.67	1.71	16.48	2.59
55505.42	4.36	19.99	8.01
55510.47	2.24	8.01	1.65
55517.29	2.26	121.44	25.21
55520.48	21.8	19.33	38.69
55520.48	2.96	135.86	36.97
55523.94	1.78	18.17	2.97
55526.5	2.69	34.52	8.53
55528.41	4.1	9.9	3.73
55529.88	3.49	22.79	7.31
55532.98	2.92	12.84	3.45
55534.56	4.14	7.61	2.9
55537.43	2.95	4.91	1.33
55541.38	4.13	16.42	6.24
55544.67	1.78	17.99	2.94
55549.41	4.13	24.79	9.41
55549.51	14.72	22.54	30.51
55552.7	1.78	15.05	2.46
55560.4	1.77	9.79	1.6
55563.12	1.56	10.78	1.55
55566.96	4.48	36.73	15.14
55575.18	5.29	11.32	5.51
55583.71	5.51	12.17	6.15
56551.59	1.96	3.01	0.12
56554.48	2.22	2.74	0.10
56556.42	1.05	1.45	0.11
56559.29	1.85	37.30	1.64
56560.84	5.01	40.64	0.66
56565.77	1.92	4.82	0.20
56568.30	2.01	5.71	0.23
56571.37	2.58	3.63	0.11
56798.48	2.95	5.45	1.47
56801.55	2.6	3.95	0.94
56804.45	2.54	4.03	0.94
56808.08	2.84	5.56	1.45
56810.65	1.25	7.82	0.9
56812.89	1.99	7.89	1.44
56816.42	1.89	20.99	3.64
56823.01	4.4	53.22	21.52
56827.51	1.1	31.67	3.2
56831.13	3.37	66.52	20.59
56834.57	1.27	46.65	5.43
56836.13	1.73	21.85	3.48

**Table 1** — *Continued.*

Center (MJD)	FWHM (d)	$L_{\text{peak}}$ ( $10^{48} \text{ erg s}^{-1}$ )	$E_{\gamma}$ ( $10^{54} \text{ erg}$ )
56839.09	2.2	12.76	2.58
56842.28	3.03	11.27	3.14
56846.32	2.91	7.95	2.13
56848.45	1.07	4.85	0.48
56850.57	2.19	6.76	1.15
56861.74	1.6	1.78	0.25
56865.21	1.48	15	2.04
56868.74	1.91	12.26	2.15
56872.48	1.69	38.77	6.04
56874.15	1.55	4.6	0.65
56876.16	0.96	3.84	0.34
56878.48	2.12	2.2	0.43
56883.53	1.61	13.42	1.99
56886.23	1.64	19.16	2.89
56909.29	2.83	8.1	2.08
56912.46	1.43	6.94	0.91
56914.53	1.44	12.72	1.69
56916.5	1.04	36.43	3.48
56919.75	2.26	9.2	1.92
56924.88	1.65	5.94	0.9
56928.01	2.49	6.18	1.42
56932.09	2.84	3.88	1.01
56961.51	1.68	8.92	1.38
56966.06	3.6	8.04	2.67
56974.45	1.67	7.46	1.15
56986.58	8.04	3.45	2.55
56988.2	2.7	8.28	2.05
57007.17	6.93	8.7	5.54
57008.7	0.8	6.52	0.48
57015.41	1.6	3.56	0.52
57019.4	4.24	4.25	1.66
57022.91	1.75	3.69	0.59
57028.27	4.54	3.61	1.49
57056.25	2.52	5.11	1.18
57058.81	1.35	14.66	1.82
57060.13	1.57	8.38	1.21
57062.09	2.58	13.38	3.17
57065.53	1.26	2.27	0.26
57068.86	2.31	6.85	1.46
57070.5	7.08	3.76	2.45
57076.28	3.49	3.04	0.98
57080.49	2.26	4.18	0.87
57082.97	1.84	7.61	1.29
57087.06	4.5	3.37	1.4
57089.49	1.42	3.54	0.46
57091.44	1.78	5.4	0.88
57093.54	1.39	4.43	0.57
57095.44	2.26	3.45	0.72
57102.7	5.99	13.94	7.69
57113.01	4.39	3.31	1.34
57119.83	4.69	1.42	0.59
57144.44	2.02	1.88	0.34
57147.86	2.1	3.47	0.67
57153.39	2.71	14.36	3.58
57171.39	1.68	2.51	0.39
57174.55	1.51	9.52	1.32
57176.12	0.9	10.11	0.84
57178.48	2.25	7.33	1.52
57181.44	3.3	2.41	0.73
57185.57	0.84	8.1	0.63
57188.45	1.66	3.34	0.51

**Table 1** — *Continued.*

Center (MJD)	FWHM (d)	$L_{\text{peak}}$ ( $10^{48} \text{ erg s}^{-1}$ )	$E_{\gamma}$ ( $10^{54} \text{ erg}$ )
57190.48	0.73	2.33	0.16
57192.69	2.51	5.17	1.19
57198.5	3.43	11.38	3.59
57203.23	2.32	6.4	1.36
57204.42	1.21	30.52	3.39
57206.6	1.57	18.2	2.62
57209.35	2.46	2.45	0.54
57246	5.23	4.24	2
57249.8	2.16	5.44	1.08
57255.3	4.55	38.58	16.15
57264.33	1.82	4.37	0.73
57268.46	2.86	6.47	1.7
57271.51	2.12	6.69	1.3
57273.91	1.64	4.88	0.74
57276.58	3.15	5.01	1.45
57279.09	1.84	15.39	2.6
57281.61	1.06	5.29	0.52
57285.28	4.29	3	1.18
57288.68	2.07	4.8	0.92
57290.85	1.75	4.8	0.77
57294.55	3.5	6.4	2.06
57298.01	1.61	4.6	0.68
57299.57	1.94	4.28	0.76
57302.47	2.18	12.29	2.47
57305.95	2.38	3.17	0.69
57311.13	4.35	4.72	1.89
57315.66	2.89	6.79	1.81
57319.09	3.11	1.97	0.56
57324.81	5.79	9.07	4.83
57326.61	1.39	7.29	0.93
57332.14	4.96	6.72	3.06
57337.6	2.07	5.98	1.14
57341.64	3.03	9.02	2.51
57345.45	2.15	7.65	1.51
57351.55	11.96	2.77	3.01
57353.69	1.88	4.36	0.75
57376.5	2.66	1.09	0.26
57380.04	2.06	2.13	0.4
57383.5	1.9	2.12	0.37
57387.5	2.68	7.07	1.74
57391.65	3.63	5.71	1.9
57394.42	1.09	3.07	0.31
57396.47	4.09	5.19	1.95
57401.8	3.23	10.56	3.13
57407.25	4.37	12.81	5.15
57411.41	1.76	1.84	0.3
57413.5	0.97	2.45	0.22
57417	6.27	5.64	3.25
57419.46	0.81	1.96	0.15
57422.49	2.71	3.5	0.87
57424.5	0.77	2.73	0.19
57426.47	2.65	6.22	1.52
57428.5	1.22	3.1	0.35
57430.93	4.71	3.46	1.35

also given in Figure 8. It is found that the gamma-ray flux is correlated with the fluxes in the *R*-band and X-ray band, and is weakly correlated with the radio flux. No clear correlation between the gamma-ray flux and

the evolution of the optical linear polarization degree is found for the global and second segment lightcurves, but they are correlated during the first segment lightcurves, which are consistent with the reported results in Jorstad et al. (2010, 2013).

## 6 DISCUSSION

Several models have been proposed to explain the origin of the erratic outbursts observed in blazars. 3C 454.3 with significant spectral and flux variations should be the best candidate to study this issue. 3C 454.3 is a typical flat spectrum radio quasar (FSRQ) and its jet orientation should point to the line of sight. It was suggested that the outbursts with different brightness may be due to a helical jet, in which blobs move at different angles with respect to the line of sight leading to a different Doppler boosting effect on the observed photons (e.g., Villata et al. 2007; Jorstad et al. 2013). As we have demonstrated, the variation of gamma-ray flux is accompanied by variations in spectral index and optical polarization degree. These facts cannot simply be explained with the Doppler effect.

Several observations have revealed that the optical and gamma-ray outbursts of 3C 454.3 show a connection with a superluminal knot through the core (Jorstad et al. 2010, 2013). It is possible that the central engine of 3C 454.3 intermittently ejects the sequential blobs with different velocities, which induce multiple collisions and a series of outbursts, i.e., the complex lightcurves that are produced by superpositions of many flares with different timescales. The correlation between gamma-ray flux and optical linear polarization degree indicates that the gamma-ray emission is produced in a region with an ordered magnetic field. This may imply that the radiation regime of this FSRQ is highly magnetized (e.g., Zhang et al. 2014). Zhang & Yan (2011) proposed an internal-collision-induced magnetic reconnection and turbulence (ICMART) process to explain the prompt emission of gamma-ray bursts. This model suggests that the Poynting flux energy is converted to the energies of electrons and protons efficiently and the prompt emission is due to the synchrotron radiation of these electrons. This scenario may be consistent with the observed correlations between gamma-ray flux and optical linear polarization degree as well as the spectral index.

In addition, the typical variability timescale in the gamma-ray band derived in our analysis is several days.

The timescales of the order of 1 d or longer should be interpreted as the typical timescales of successive flare events, which may be due to the collisions of blobs in the internal shock, as discussed by Kataoka et al. (2001) for X-ray data from three BL Lacs. Nakagawa & Mori (2013) also reported that the four-year lightcurve at the GeV band of 3C 454.3 shows a specific timescale of  $6.8 \times 10^5$  s, and this value suggests a black hole mass of  $10^8$ – $10^{10} M_{\odot}$  within the framework of the internal shock models. Therefore, the magnetized shells with different velocities ejected by the central engine may collide and induce an ICMART process to accelerate the radiation particles in 3C 454.3.

Cross comparisons of the statistical properties for 3C 454.3 with other sources may give clues to the nature of these flares. Neilsen et al. (2013, 2015) analyzed X-ray flares from Sagittarius A\* and found that the cumulative distributions of the duration, luminosity and energy of the X-ray flares can be described by a power-law function, with indices of  $\alpha_T = 0.9 \pm 0.2$ ,  $\alpha_L = 1.9^{+0.4}_{-0.3}$  and  $\alpha_E = 1.5 \pm 0.2$ , respectively. Li et al. (2015) found similar results via a simulation analysis and suggested that these results are consistent with the theoretical prediction of a self-organized criticality (SOC) system with spatial dimension  $S=3$  (Aschwanden 2011, 2012, 2014). They further reported that the X-ray flares represent plasmoid ejections driven by magnetic reconnection (similar to solar flares) in the accretion flow onto the black hole. We made a similar analysis of  $\gamma$ -ray flares from 3C 454.3, as shown in Figure 9. We get  $\alpha_E = 1.46 \pm 0.02$ ,  $\alpha_L = 1.54 \pm 0.08$  and  $\alpha_T = 2.28 \pm 0.05$  (with duration time defined as four times the FWHM). The derived  $\alpha_E$  and  $\alpha_L$  are roughly consistent with those from the X-ray flares in Sagittarius A\*, but  $\alpha_T$  is much larger than that of the X-ray flares in Sagittarius A\*. Based on the Gaussian flare profile assumption that we adopt in this paper, Li et al. (2015) obtained  $\alpha_T > 2.1$  for the X-ray flares in Sagittarius A\*. Wang et al. (2015) analyzed the detected sample of Neilsen et al. (2013) with a different selection of the fitting data ranges and found  $\alpha_T = 1.9 \pm 0.5$ . These results are consistent with ours, and thus the nature of 3C 454.3 may be also consistent with the SOC system, similar to Sagittarius A\*. Therefore, the GeV flares associated with 3C 454.3 may also be from the plasmoid ejections driven by magnetic reconnection. This further supports the idea that the jet radiation regions of FSRQs may be highly magnetized (e.g., Zhang et al. 2014, 2015).

**Table 2** Data on 34 Outburst Episodes

Outbursts	Date (MJD)	Duration (d)	$L_{\max}$ ( $10^{49} \text{ erg s}^{-1}$ )	$L_{\min}$ ( $10^{48} \text{ erg s}^{-1}$ )	$\Gamma_{\max}$	$\Gamma_{\min}$	$L_{\max}/L_{\min}$	$r$	$p$	$k$
1	54714.5–54758.5	45	$1.22 \pm 0.19$	$1.50 \pm 0.34$	$-2.18 \pm 0.08$	$-2.69 \pm 0.17$	8.13	0.615	1.48e-5	$0.34 \pm 0.08$
2	55083.5–55097.5	15	$1.07 \pm 0.12$	$2.98 \pm 0.56$	$-2.32 \pm 0.08$	$-2.60 \pm 0.12$	3.59	0.404	0.152	$0.21 \pm 0.18$
3	55119.5–55142.5	24	$0.93 \pm 0.09$	$2.11 \pm 0.45$	$-2.29 \pm 0.09$	$-2.83 \pm 0.20$	4.41	0.663	5.68e-4	$0.52 \pm 0.16$
4	55151.5–55157.5	7	$1.48 \pm 0.23$	$3.41 \pm 0.65$	$-2.20 \pm 0.08$	$-2.43 \pm 0.10$	4.34	0.539	0.212	$0.29 \pm 0.21$
5	55157.5–55189.5	33	$4.20 \pm 0.30$	$6.25 \pm 0.85$	$-2.19 \pm 0.04$	$-2.56 \pm 0.06$	6.72	0.258	0.147	$0.10 \pm 0.05$
6	55189.5–55204.5	16	$1.76 \pm 0.18$	$4.63 \pm 0.72$	$-2.20 \pm 0.06$	$-2.47 \pm 0.09$	3.80	0.687	0.003	$0.32 \pm 0.12$
7	55274.5–55315.5	42	$2.77 \pm 0.17$	$2.69 \pm 0.42$	$-2.30 \pm 0.03$	$-2.70 \pm 0.17$	10.30	0.475	0.003	$0.14 \pm 0.05$
8	55315.5–55344.5	30	$1.53 \pm 0.12$	$3.63 \pm 0.60$	$-2.23 \pm 0.08$	$-2.62 \pm 0.15$	4.21	0.342	0.069	$0.14 \pm 0.09$
9	55492.5–55512.5	21	$3.13 \pm 0.28$	$6.57 \pm 0.67$	$-2.15 \pm 0.04$	$-2.58 \pm 0.10$	4.76	0.844	1.51e-6	$0.47 \pm 0.07$
10	55512.5–55525.5	14	$16.00 \pm 0.06$	$18.41 \pm 1.54$	$-2.15 \pm 0.02$	$-2.36 \pm 0.06$	8.69	0.706	6.52e-4	$0.14 \pm 0.03$
11	55525.5–55536.5	12	$6.28 \pm 0.34$	$20.35 \pm 1.41$	$-2.29 \pm 0.03$	$-2.41 \pm 0.04$	3.09	0.862	3.90e-4	$0.31 \pm 0.09$
12	55559.5–55593.5	35	$4.24 \pm 0.37$	$4.42 \pm 0.56$	$-2.21 \pm 0.04$	$-2.61 \pm 0.13$	9.59	0.574	0.227	$0.23 \pm 0.05$
13	55639.5–55649.5	11	$1.19 \pm 0.16$	$0.91 \pm 0.28$	$-2.20 \pm 0.10$	$-2.67 \pm 0.32$	13.08	0.668	0.028	$0.25 \pm 0.14$
14	56386.5–56394.5	9	$1.20 \pm 0.30$	$0.69 \pm 0.21$	$-1.84 \pm 0.21$	$-2.74 \pm 0.36$	17.39	0.524	0.227	$0.42 \pm 0.25$
15	56555.5–56569.5	15	$2.56 \pm 0.51$	$2.01 \pm 0.65$	$-1.81 \pm 0.06$	$-2.73 \pm 0.21$	12.74	0.750	0.001	$0.61 \pm 0.10$
16	56814.5–56818.5	5	$2.17 \pm 0.25$	$4.38 \pm 0.72$	$-2.18 \pm 0.06$	$-2.51 \pm 0.14$	4.95	0.992	8.65e-4	$0.53 \pm 0.17$
17	56818.5–56826.5	9	$5.46 \pm 0.49$	$6.35 \pm 0.81$	$-2.03 \pm 0.04$	$-2.49 \pm 0.10$	8.60	0.756	0.018	$0.34 \pm 0.08$
18	56828.5–56833.5	6	$6.60 \pm 0.56$	$16.30 \pm 2.14$	$-1.95 \pm 0.04$	$-2.11 \pm 0.06$	4.05	0.870	0.024	$0.24 \pm 0.09$
19	56833.5–56837.5	5	$5.28 \pm 0.83$	$5.81 \pm 0.11$	$-1.93 \pm 0.05$	$-2.24 \pm 0.10$	9.09	0.847	0.074	$0.32 \pm 0.13$
20	56870.5–56875.5	6	$1.98 \pm 0.43$	$6.50 \pm 0.13$	$-1.89 \pm 0.08$	$-2.58 \pm 0.19$	3.04	0.877	0.022	$0.70 \pm 0.22$
21	56880.5–56888.5	9	$2.25 \pm 0.62$	$4.99 \pm 1.95$	$-2.02 \pm 0.11$	$-2.71 \pm 0.20$	4.51	0.931	7.74e-4	$1.02 \pm 0.31$
22	56906.5–56911.5	6	$0.96 \pm 0.25$	$1.87 \pm 0.77$	$-2.19 \pm 0.13$	$-2.59 \pm 0.21$	5.13	0.735	0.096	$0.67 \pm 0.48$
23	56915.5–56917.5	3	$3.84 \pm 0.84$	$5.28 \pm 0.11$	$-1.94 \pm 0.07$	$-2.53 \pm 0.18$	7.27	0.980	0.127	$0.66 \pm 0.20$
24	56917.5–56922.5	6	$1.11 \pm 0.34$	$2.14 \pm 0.62$	$-2.12 \pm 0.14$	$-3.36 \pm 0.53$	5.19	0.921	0.009	$1.68 \pm 0.70$
25	56971.5–56979.5	9	$0.92 \pm 0.55$	$1.54 \pm 0.62$	$-1.80 \pm 0.19$	$-2.72 \pm 0.41$	5.97	0.968	3.38e-4	$1.20 \pm 0.56$
26	56979.5–56991.5	13	$1.25 \pm 0.24$	$1.79 \pm 0.60$	$-2.05 \pm 0.17$	$-2.79 \pm 0.29$	6.98	0.712	0.009	$0.70 \pm 0.29$
27	57002.5–57014.5	13	$1.56 \pm 0.15$	$3.50 \pm 0.47$	$-2.22 \pm 0.08$	$-2.70 \pm 0.14$	4.46	0.573	0.052	$0.33 \pm 0.14$
28	57024.5–57032.5	9	$0.57 \pm 0.12$	$1.64 \pm 0.31$	$-2.23 \pm 0.11$	$-2.95 \pm 0.26$	3.48	0.842	0.004	$1.09 \pm 0.44$
29	57052.5–57064.5	13	$1.73 \pm 0.26$	$1.11 \pm 0.35$	$-2.01 \pm 0.07$	$-2.87 \pm 0.21$	15.59	0.853	2.12e-4	$0.61 \pm 0.11$
30	57275.5–57282.5	8	$1.69 \pm 0.20$	$2.33 \pm 0.48$	$-2.11 \pm 0.07$	$-2.53 \pm 0.18$	7.25	0.707	0.050	$0.39 \pm 0.14$
31	57300.5–57304.5	5	$1.29 \pm 0.15$	$2.64 \pm 0.67$	$-2.27 \pm 0.07$	$-2.56 \pm 0.12$	4.89	0.546	0.341	$0.39 \pm 0.24$
32	57321.5–57329.5	9	$1.41 \pm 0.15$	$3.31 \pm 0.48$	$-2.14 \pm 0.08$	$-2.64 \pm 0.15$	4.26	0.837	0.005	$0.63 \pm 0.19$
33	57349.5–57362.5	14	$0.77 \pm 0.13$	$0.83 \pm 0.26$	$-2.14 \pm 0.14$	$-2.87 \pm 0.33$	9.28	0.718	0.004	$0.56 \pm 0.23$
34	57381.5–57412.5	32	$1.37 \pm 0.16$	$1.27 \pm 0.27$	$-2.21 \pm 0.08$	$-2.91 \pm 0.28$	10.79	0.490	0.006	$0.30 \pm 0.11$

## 7 SUMMARY

We have analyzed the  $\gamma$ -ray long-term lightcurve observed with *Fermi*/LAT, and collected simultaneous lightcurves in the radio, optical and X-ray bands of 3C 454.3 from the literature. Our results are summarized below.

- (1) The flux variation of 3C 454.3 in the  $\gamma$ -ray band is correlated with the flux variation in the *R*-band and X-ray band, and a weak correlation between gamma-ray flux and radio flux is also observed, indicating that the radiations at these energy bands are co-spatial.
- (2) The PDS of the global lightcurve in the  $\gamma$ -ray band is fitted with a broken power-law and yields an obvious turnover at  $\sim 7.7$  d, which may indicate a typical variability timescale of 3C 454.3 in the  $\gamma$ -ray band.
- (3) The spectral evolutions accompanying the flux variations in the  $\gamma$ -ray band are observed, showing the behavior of “harder when brighter.”
- (4) The spectral evolution and an increase of the optical linear polarization degree along with the increase of the  $\gamma$ -ray flux may imply that the radiation particles are accelerated and the magnetic field is ordered by the shock processes. The nature of 3C 454.3 may be consistent with an SOC system, and thus the  $\gamma$ -ray

outbursts are from the plasmoid ejections driven by magnetic reconnection.

**Acknowledgements** We thank the helpful discussion with Wei Cui, Shuang-Nan Zhang, Yuan Liu and Da-Bin Lin. This study makes use of radio, optical and X-ray data from the VLBA-BU Blazar Monitoring Program (VLBA-BU-BLAZAR; <http://www.bu.edu/blazars/VLBAproject.html>), funded by NASA through the Fermi and Swift Guest Investigator Programs. This research has made use of data from the OVRO 40-m monitoring program (Richards, J. L. et al. 2011, ApJS, 194, 29) which is supported in part by NASA (Grants NNX08AW31G, NNX11A043G) and NNX14AQ89G and NSF (Grants AST-0808050 and AST-1109911). This work is supported by the National Natural Science Foundation of China (Grant Nos. 11573034, 11533003, 11363002, 11373036, 11463001 and U1731239), the National Basic Research Program of China (973 Programme, Grant 2014CB845800), and En-Wei Liang acknowledges support from special funding from the Guangxi Science Foundation for Guangxi Distinguished Professors (Bagui Yingcai & Bagui Xuezheng).

## References

- Abdo, A. A., Ackermann, M., Ajello, M., et al. 2010, *Nature*, 463, 919
- Abdo, A. A., Ackermann, M., Ajello, M., et al. 2011, *ApJ*, 733, L26
- Ackermann, M., Ajello, M., Baldini, L., et al. 2010, *ApJ*, 721, 1383
- Ackermann, M., Ajello, M., Atwood, W. B., et al. 2015, *ApJ*, 810, 14
- Aleksić, J., Antonelli, L. A., Antoranz, P., et al. 2011, *ApJ*, 730, L8
- Arlen, T., Aune, T., Beilicke, M., et al. 2013, *ApJ*, 762, 92
- Aschwanden, M. J. 2011, *Self-Organized Criticality in Astrophysics* (Berlin: Springer-Praxis)
- Aschwanden, M. J. 2012, *A&A*, 539, A2
- Aschwanden, M. J. 2014, *ApJ*, 782, 54
- Britto, R. J., Bottacini, E., Lott, B., Razzaque, S., & Buson, S. 2016, *ApJ*, 830, 162
- Chen, L. 2017, *ApJ*, 842, 129
- Cui, W. 2004, *ApJ*, 605, 662
- Edelson, R. A., & Krolik, J. H. 1988, *ApJ*, 333, 646
- Fossati, G., Buckley, J. H., Bond, I. H., et al. 2008, *ApJ*, 677, 906
- Ghisellini, G., & Tavecchio, F. 2008, *MNRAS*, 386, L28
- Hong, S., Xiong, D., & Bai, J. 2017, arXiv:1711.08641
- Jorstad, S. G., Marscher, A. P., Larionov, V. M., et al. 2010, *ApJ*, 715, 362
- Jorstad, S. G., Marscher, A. P., Smith, P. S., et al. 2013, *ApJ*, 773, 147
- Kataoka, J., Takahashi, T., Wagner, S. J., et al. 2001, *ApJ*, 560, 659
- Larionov, V. M., Villata, M., & Raiteri, C. M. 2010, *A&A*, 510, A93
- Lehto, H. J., & Valtonen, M. J. 1996, *ApJ*, 460, 207
- Li, Y.-P., Yuan, F., Yuan, Q., et al. 2015, *ApJ*, 810, 19
- Liao, N.-H., Xin, Y.-L., Fan, X.-L., et al. 2016, *ApJS*, 226, 17
- Lomb, N. R. 1976, *Ap&SS*, 39, 447
- Massaro, F., Tramacere, A., Cavaliere, A., Perri, M., & Giommi, P. 2008, *A&A*, 478, 395
- Nakagawa, K., & Mori, M. 2013, *ApJ*, 773, 177
- Nalewajko, K. 2013, *MNRAS*, 430, 1324
- Neilsen, J., Nowak, M. A., Gammie, C., et al. 2013, *ApJ*, 774, 42
- Neilsen, J., Markoff, S., Nowak, M. A., et al. 2015, *ApJ*, 799, 199
- Pacciani, L., Tavecchio, F., Donnarumma, I., et al. 2014, *ApJ*, 790, 45
- Raiteri, C. M., Villata, M., Aller, M. F., et al. 2011, *A&A*, 534, A87
- Richards, J. L., Max-Moerbeck, W., Pavlidou, V., et al. 2011, *ApJS*, 194, 29
- Scargle, J. D. 1982, *ApJ*, 263, 835
- Sillanpaa, A., Haarala, S., Valtonen, M. J., Sundelius, B., & Byrd, G. G. 1988, *ApJ*, 325, 628
- Sillanpaa, A., Takalo, L. O., Pursimo, T., et al. 1996, *A&A*, 305, L17
- Tramacere, A., Giommi, P., Perri, M., Verrecchia, F., & Tosti, G. 2009, *A&A*, 501, 879
- Vaughan, S. 2010, *MNRAS*, 402, 307
- Villata, M., Raiteri, C. M., Aller, M. F., et al. 2007, *A&A*, 464, L5
- Wang, F. Y., Dai, Z. G., Yi, S. X., & Xi, S. Q. 2015, *ApJS*, 216, 8
- Wehrle, A. E., Marscher, A. P., Jorstad, S. G., et al. 2012, *ApJ*, 758, 72
- Zhang, B., & Yan, H. 2011, *ApJ*, 726, 90
- Zhang, J., Liang, E.-W., Zhang, S.-N., & Bai, J. M. 2012, *ApJ*, 752, 157
- Zhang, J., Zhang, S.-N., & Liang, E.-W. 2013, *ApJ*, 767, 8
- Zhang, J., Sun, X.-N., Liang, E.-W., et al. 2014, *ApJ*, 788, 104
- Zhang, J., Xue, Z.-W., He, J.-J., Liang, E.-W., & Zhang, S.-N. 2015, *ApJ*, 807, 51
- Zhu, Y. K., Zhang, J., Zhang, H. M., et al. 2016, *RAA (Research in Astronomy and Astrophysics)*, 16, 170